Optics & Laser Technology 192 (2025) 113415

Contents lists available at ScienceDirect

Optics and Laser Technology

journal homepage: www.elsevier.com/locate/jolt

Full length article

Advancing VCSEL integration with femtosecond laser microstructuring and 3D nanoprinting

Athanasios Kyriazis [a,b,*], Salah Guessoum [a,b], Jeroen Missinne [a], Martin Virte [b], Jürgen Van Erps [b], Geert Van Steenberge [a]

[a] Center for Microsystems Technology (CMST), Ghent University and imec, Technologiepark-Zwijnaarde 126, Ghent, 9052, Belgium
[b] Brussels Photonics (B-PHOT), Dept. of Applied Physics and Photonics, Vrije Universiteit Brussel and Flanders Make, Pleinlaan 2, Brussel, 1050, Belgium

ARTICLE INFO

Keywords:
Femtosecond laser irradiation
Chemical etching
Two-photon polymerization
Beam shaping
VCSEL integration
Fused silica interposer
Optoelectronic packaging

ABSTRACT

With increasing demands on data processing speeds and the correspondingly high requirements for data transfer bandwidth, research is focusing on replacing pluggable optical transceivers with co-packaged optics architectures. Vertical-cavity surface-emitting lasers (VCSELs) have been considered a promising candidate in such configurations, but traditional optoelectronic packaging approaches—such as flip-chip and wire-bonding—fall short of meeting the low-cost and high-speed requirements. In this paper, we present the integration of bare-die VCSEL arrays into femtosecond laser-fabricated fused silica microwells, combined with direct on-VCSEL fabrication of micro-optics using two-photon polymerization-based direct laser writing. The 1×4 VCSEL arrays, operating at a wavelength of 850 nm, are aligned in a face-up configuration and are electrically interconnected within a 5.5 μm passivation layer with photolithographically defined copper tracks. Efficient beam shaping is demonstrated by 3D nanoprinting 200 μm tall refractive and diffractive focusing microlenses directly onto the integrated VCSELs with an in-plane pitch of 250 μm. The emitted beams are focused into a 5 μm diameter Gaussian spot and are efficiently coupled into a single-mode fiber. This scalable packaging approach highlights the potential for compact, high-density solutions for co-packaged optics architectures with glass interposers.

1. Introduction

1.1. Background

The rapid growth of data traffic in data centers—driven, among others, by high-performance computing, artificial intelligence applications, and cloud-based services—has intensified the need for advanced optical transceiver technologies. To address these needs, optical packaging has shifted toward co-packaged optics (CPO) architectures, offering high bandwidth, increased integration density, low latency, cost-effectiveness, and improved energy efficiency [1]. Parallel to silicon photonics research, which aims to leverage existing complementary metal-oxide-semiconductor infrastructure for creating photonic integrated circuits [2], there is increasing interest in VCSEL-based CPO solutions. Researchers have identified cost and power efficiency as key strengths of this approach [3,4], supported by advancements in VCSEL-based transceiver research [5–12]. Nevertheless, VCSEL-based CPO remains in the research and development phase, with packaging challenges standing as a primary barrier to its wider adoption [13].

An important element of the packaging approach is the material of the interposer, which serves as the base platform for integrating VCSELs, photodetectors, and application-specific integrated circuits. Glass is frequently chosen due to its high thermal stability, electrical insulation, and precise dimensional control for optical alignment [13,14]. The integration of through-glass vias further enhances these advantages by enabling compact and efficient electrical interconnections [15]. While the relatively low thermal conductivity of glass might pose a challenge, solutions such as incorporating metal layers for heat dissipation and optimizing cooling microvias have shown potential for mitigating these limitations [16]. Furthermore, successful integration of VCSELs on glass interposers has been demonstrated, keeping glass in the foreground [17,18].

Another aspect of the CPO architecture is the spatial arrangement of the optoelectronic components with respect to the surrounding chips and the interposer. Firstly, flip-chip bonding has been used for its scalability potential and ease of assembly and has been leveraged to integrate photonic integrated circuits on glass in CPO architectures [19]. Although flip-chip has been reliably demonstrated on glass for VCSELs

* Corresponding author at: Center for Microsystems Technology (CMST), Ghent University and imec, Technologiepark-Zwijnaarde 126, Ghent, 9052, Belgium.
Email address: Athanasios.Kyriazis@Ugent.be (A. Kyriazis).

https://doi.org/10.1016/j.optlastec.2025.113415
Received 24 March 2025; Received in revised form 22 May 2025; Accepted 18 June 2025
Available online 24 June 2025

as well [20], it renders the emission region inaccessible for further processing and limits the optical coupling options. One alternative is flip-chip bonding of VCSELs emitting through the backside—which has been demonstrated for longer wavelengths than the conventional 850 nm [6,9,10]. However, bottom-emitting chips are not yet standardized. Furthermore, face-up assembly with wire-bonding—as in [21], for instance—is generally unsuitable for CPO due to the physical complexity of the interconnect layout—requiring out-of-plane arcs—and its limitations in complying with high-density and high-speed requirements [22].

1.2. Integration and technology overview

In this paper, we propose a packaging scheme consisting of face-up VCSEL integration in glass, followed by the fabrication of micro-optical elements on top of the VCSELs (Fig. 1). More specifically, we use femtosecond laser irradiation assisted chemical etching (FLICE) to create microwells at the surface of a fused silica substrate. The microwells act as housing receptacles in which the VCSEL arrays are precisely placed and bonded. An electrical redistribution layer (ERDL) is created, i.e. a galvanic fan-out to connect the small-scale VCSEL pads (μm-scale) to the larger-scale driver instrumentation (mm-scale). The ERDL formation steps entail spin-coating of a passivation layer, microvia drilling, metal sputtering and photolithography, similar to previously reported work [23,24]. At this stage, the VCSEL arrays have been fully packaged and the emitted beams are characterized. The characterized beam information is used to design two focusing microlens counterparts (refractive and diffractive) for single-mode fiber (SMF) coupling. To demonstrate efficient beam shaping, the microlenses are subsequently fabricated on the packaged VCSEL arrays using two-photon polymerization-based direct laser writing (2PP-DLW). Finally, the focused beams are characterized and subsequently coupled into SMFs. Contrary to wire-bonding-based solutions [21,25], this assembly approach maintains the flip-chip benefits, whilst allowing direct access to the VCSEL emission region, and can be used with standard chips with top contacts without the need for intricate custom designs, hence reducing both time and cost.

As described above, the two core technologies that synergistically facilitate the proposed integration process are FLICE and 2PP-DLW. Generally, laser-based light-matter interaction has long been a valuable tool for the precise modification of dielectric materials, enabling processes such as ablation [26] and welding [27]. Specifically for FLICE and 2PP-DLW, laser irradiation is delivered in the form of ultrashort pulses. In FLICE, as the pulse durations approach the femtosecond scale, nonlinear photon absorption enables spatially confined material modification without inducing heat transfer or damage to the surrounding area [28]. By focusing femtosecond laser pulses in fused silica glass, researchers have successfully fabricated waveguides [29] and later combined this approach with chemical etching to create 3D geometries in amorphous silica [30]. The mechanism of FLICE is primarily believed to be attributed to the formation of nanogratings [31], along which etching is greatly accelerated while leaving unexposed regions effectively (but not entirely) unaltered. KOH is often the preferred etching agent due to its high selectivity [32] and has been widely utilized in recent applications [33–35]. Similarly, non-linear photon absorption in the femtosecond pulse regime is utilized in 2PP-based DLW [36]. A near-infrared beam is tightly focused into the bulk of a liquid, negative-tone photoresist, locally solidifying it by a polymerization interaction initiated by two-photon absorption (approximately $200 \times 200 \times 500\ \mathrm{nm}^3$ voxel size). By raster-scanning the focal spot in a layer-wise fashion within the photoresist volume, 3D structures can be realized in the sub-micrometer

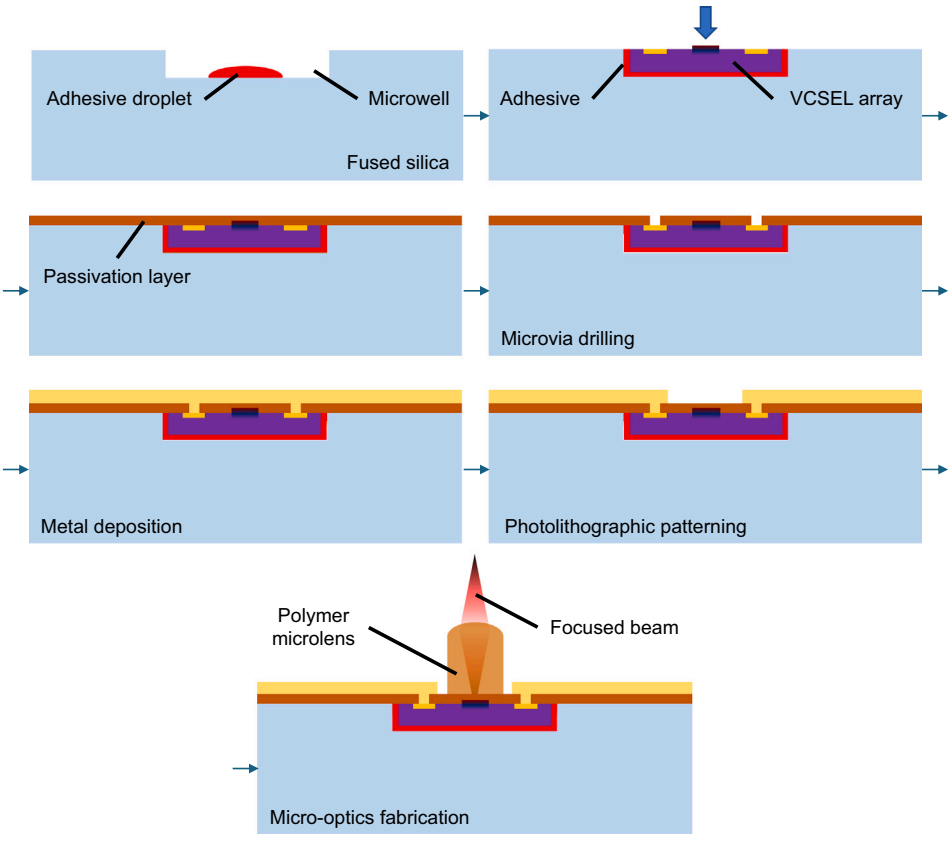

Fig. 1. Cross-sectional illustration of the chip and micro-optics integration process. First, a microwell is formed using femtosecond laser irradiation assisted chemical etching. Subsequently, adhesive is deposited and the VCSEL chip is fitted into the microwell. A passivation layer is then spin-coated, followed by laser drilling of microvias for interconnects. Metal sputtering is used to deposit conductive layers, and photolithographic patterning defines the galvanic tracks for electrical connectivity. Finally, beam shaping micro-optics are 3D-nanoprinted on top of the integrated VCSELs.

scale [37]. This technique allows for quick prototyping cycles, offers great flexibility in the design of the beam-shaping elements, and has therefore been extensively used in the fabrication of various micro-optic elements, such as photonic wire-bonds [38], free-form holograms [39], planar waveguides [40], refractive microlens stacks [41], and meta-lenses [42].

The paper is structured as follows. In Section 2, we present the use of FLICE to optimize the fabrication of microwells on the surface of fused silica. We detail the embedding and electrical interconnection of the VCSEL arrays within the microwells, followed by the characterization of their emission characteristics. In Section 3, we describe the design of refractive and diffractive focusing microlenses for coupling the beam emitted by the VCSELs into SMFs. In Section 4, we present the fabrication of the microlenses directly on the chip, after optimizing the 2PP fabrication process on planar glass substrates. Then, we characterize the focused beam profiles to evaluate the performance of the integrated microlenses. Finally, we evaluate the coupling efficiency of the focused beams into an SMF for both the refractive and diffractive designs.

2. Integration of optoelectronic devices

2.1. Optimization of surface microwells for VCSEL integration

For the FLICE exposure step, we used a 1030 nm Satsuma laser (from Amplitude Laser), with a second harmonic generation module, housed in the microSTRUCT-vario platform (3D MICROMAC), along with a series of optical components for beam shaping. Most importantly, a half-wave plate and a quarter-wave plate were used to tune the polarization and a 40×, numerical aperture (NA) 0.55 objective lens (5722-A-H by Newport) was used to focus the beam onto the working plane of a motorized stage, allowing to move the sample with sub-micrometer precision. For the experiments discussed below, we used circular polarization, a pulse duration of ≈300 fs and a repetition rate of 500 kHz.

To accommodate the 1 × 4 VCSEL arrays (from Vertically Integrated Systems), cuboid microwells were fabricated on the surface of fused silica glass, using FLICE. The microwell design dimensions were initially tailored to the chips' (nominal) footprint of approximately 1 mm × 250 μm with a thickness of 150 μm. The in-plane dimensions were extended by 10–20 μm to provide a narrow margin for precise chip placement. To accommodate a thin dispensed adhesive layer beneath the chips, the microwell depth was set to be ≈10 μm greater than the chip thickness.

Although the etching time is an order of magnitude longer than the laser exposure step for our microwells, the latter remains the processing bottleneck. This is because multiple samples can be etched in parallel, whereas laser modification is a sequential process—although recent research aims to achieve laser processing parallelization, as well [43]. Thus, the primary goal of our FLICE optimization was to minimize exposure time while ensuring precise shape definition and preventing crack formation.

Firstly, the desired 3D cuboid shape was defined by following an outline inscription approach (only the base and sidewalls), rather than exposing the entire volume, effectively minimizing the lasing time (see Fig. 2). The base thickness was set to ≈10 μm, filled with 3–4 parallel planes, alternating between horizontal and vertical in-plane lines. The 20 μm wide sidewall contours consist of outlines with 2 μm in-plane pitch, connected by 30 μm radius arcs instead of sharp vertices. Theses contours are replicated out-of-plane connecting the top of the base to the surface. This allows the etchant to penetrate first through the four sidewalls and then diffuse through the base (under-etching), eventually detaching the unexposed block from the glass bulk.

Parallelly, the laser inscription parameters were optimized, focusing on the focal spot scanning speed (defined by the relative movement of the motorized stage under the focused laser beam) and the laser exposure average power. Reducing the scanning speed generally improved trajectory accuracy—minimizing the momentum from the moving stage inertia—achieving an excellent match (<1 μm) between the written lines and the design. However, reducing the speed below ≈1 mm/s provided no further observable improvement and increased exposure times. Therefore, the final scanning speed was set to 1 mm/s. On the other hand, increasing the power generally accelerated subsequent etching, but also led to after-exposure cracks at higher power levels. At a scanning speed of 1 mm/s, crack formation was observed at average powers of ≈60 mW or higher. Therefore, the average power was set to 50 mW. Accordingly, replacing sharp corners with rounded counterparts, reduced the transferred energy density, thereby lowering the induced stress in the glass bulk [44], and eliminating crack formation. The final laser exposure duration achieved for each microwell was 35 min. Process repeatability was demonstrated by fabricating more than 50 microwells under these conditions, consistently achieving defect-free results.

Finally, the microwell was formed after the sample was submerged in aqueous KOH solution (30 % w/v, at 85 °C) for 8–12 h (Fig. 3). As expected, despite its high selectivity, unexposed SiO_2 was still etched at a significantly slower, but non-negligible rate. This, combined with the progressive etching from the sidewalls to the base, led to foreseen, systematic differences between the inscribed outline and the substracted volume extent, which can be summarized as follows: (a) lateral expansion of the shape outline at the glass surface, (b) a reduction in the microwell depth, and (c) a narrower floor compared to the surface outline (shape tapering out-of-plane). The first was quantified by intermediate microscopy measurements during etching. Specifically, the length and width at the surface plane increased at a rate of ≈1 μm/h. The average depth was measured with white-light interferometry (WLI) and was found to be ≈5 μm smaller than the inscribed contour. The floor topography exhibits a height variation of ≈4 μm and a surface roughness of ≈0.5 μm. For quantifying the tapering effect, the glass was diced and the cross-section was examined microscopically. The length and width at the base plane were found to be 8 ± 2 μm and 5 ± 1 μm smaller than at the surface plane, respectively (average ± standard deviation, across 12 microwells). Finally, by adjusting the design accordingly, the target surface outline and average depth were achieved with an accuracy of 1 μm, which is comparable to the focused fs-beam spot size. Residual tapering and floor surface topography were found to have no measurable impact on subsequent integration steps and were therefore not adjusted for.

2.2. VCSEL integration in fused silica

2.2.1. Chip embedding

The steps we followed for embedding the VCSEL arrays into the fabricated microwells are schematically shown in Fig. 1. To secure the chips within the microwells, the thermally curable two-component epoxy 353ND by EPOTEK was used. This adhesive was chosen for its high-temperature resistance of up to 350 °C, which is required for the curing of the passivation layer in subsequent processing steps (Section 2.2.2). The dispensing technique was a combination of screen printing and pin transfer [45,46]. Using polyimide (PI) foils as spacers on a carrier substrate, a 75 μm adhesive layer was formed, through which a pin was swept, accumulating a droplet around the tip. Subsequently, the pin was inserted into the microwell, transferring the adhesive to the base and inner walls. The face-up assembly of the VCSEL into the cavity was done using a TRESKY flip-chip bonder. The chip was picked up by a vacuum chuck, and a split-view camera facilitated accurate alignment between the chip and the microwell. The chip was then lowered into the recess until a certain force feedback (≥10 mN) was sensed by the integrated force sensor. Finally, the adhesive was cured at 150 °C for 1 h.

With the chip securely bonded, we proceeded with the characterization of its orientation and placement accuracy. The topography of the embedded array and the surrounding glass surface was measured using WLI, allowing us to quantify the chip's tilt, tip, and maximum feature protrusion (MFP) relative to the glass surface. To ensure complete coating in the next step, an upper threshold of 5 μm was set

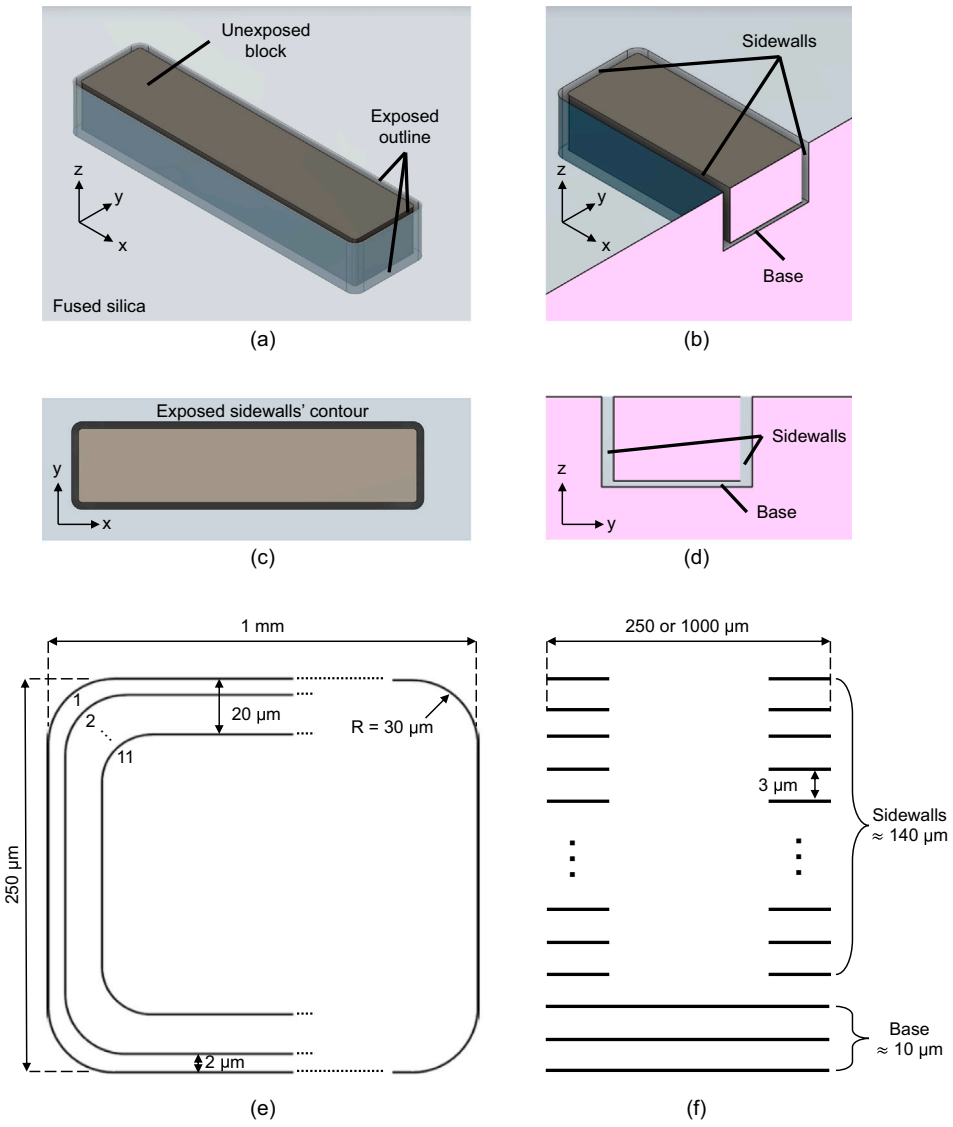

Fig. 2. Overview of the optimized outline inscription approach. In (a), the substrate and the laser-exposed outline are depicted in an isometric view. For illustration purposes, the unexposed block is shown in a darker shade, and the exposed outline appears to be already etched. In (b), a cross-section cut (in pink) is used to visualize the base and the sidewalls, which are more clearly shown in a sectional view in (d). (c) Top view of the substrate. (e) and (f) depict the laser trajectories in detail and correspond to the views of (c) and (d), respectively (not to scale). More specifically, the sidewalls' contour in (e) is replicated out-of-plane layer-wise to create the sidewalls. Accordingly, the inter-layer structure geometry is depicted in (f).

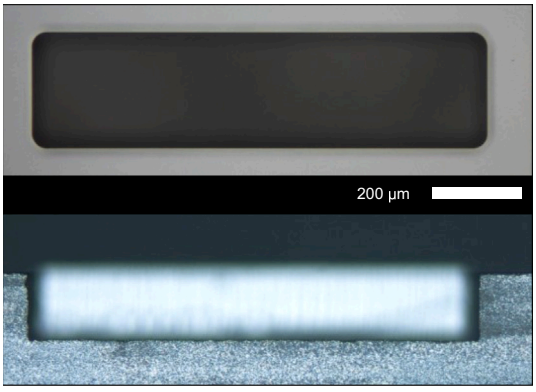

Fig. 3. Microscope images of a fully formed cuboid microwell on the surface of fused silica, after etching in KOH for 8 h. The top view surface outline is shown (top), as well as the diced cross-section (bottom).

for the MFP, based on the nominal thickness of a spin-coated PI layer (5.5 µm). The MFP was measured to be 2.4 ± 1.1 µm (n = 10), meeting this criterion, and the tip/tilt angles did not exceed 0.4°, consistently confirming precise placement (Fig. 4).

2.2.2. Electrical interconnection

For the ERDL formation, PI was selected as the passivation layer material due to its compatibility with the various requirements of the substrate and chip materials, as well as the subsequent processing steps. Specifically, the PI we used (PI-2611 from HD Microsystems) exhibits adequate adhesion to the glass substrate after silanization with (3-Aminopropyl)triethoxysilane, and possesses a low coefficient of thermal expansion. This minimizes delamination risk due to thermal variations during its own curing, subsequent processing, and VCSEL operation. Furthermore, it is suitable for via ablation and provides an excellent medium for photolithography and wet etching, as it does not react with photoresists, developers, metal etchants, or stripping solvents.

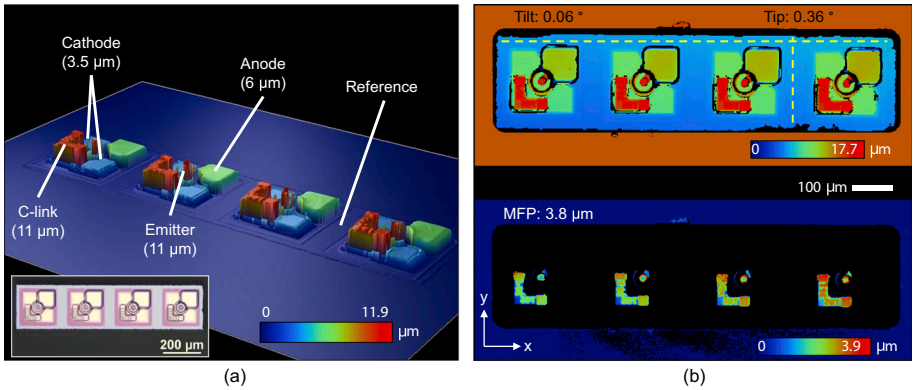

Fig. 4. WLI measurements of the chip topography before and after embedding in the fused silica microwell. (a) Perspective view of the bare chip, showing pronounced topography variations; the inset displays a top microscope view. (b) Characterization of the embedding accuracy, with tilt measured along the X-axis and tip measured along the Y-axis. Due to height differences, some features protrude above the glass surface plane, while most of the chip remains below. The MFP is extracted by masking out areas below this plane.

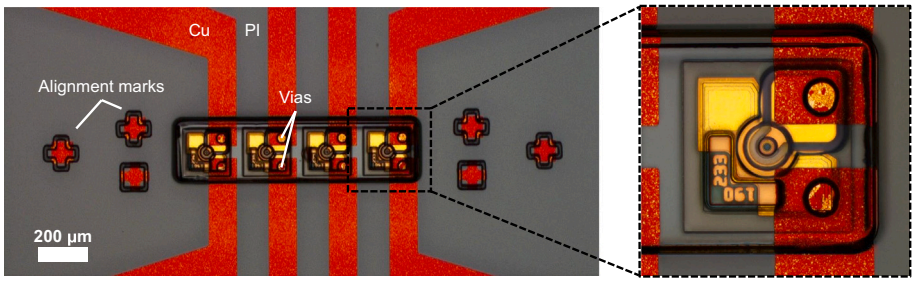

Fig. 5. Embedded 1 × 4 VCSEL array with patterned ERDL fanout (Cu), in a 25 × 25 mm^2 square fused silica sample. For each of the four VCSELs, the anode (upper side) and the cathode are connected. The alignment marks are defined with the picosecond-laser in the same step as the via opening, for increased lithography accuracy. Albeit metalized, the PI-filled, recessed regions between the chip and the glass surface are oblique, making it hard to capture with optical microscopy, and appear as dark bands.

First, PI was dropcasted on top of the silanized substrate with the embedded chip, followed by a settling time of 10 min to ensure the PI filled the potential gaps between the chip, the microwell sidewalls, and the cured epoxy. Afterwards, a 5.5 µm PI layer was formed by spin-coating and was cured by gradually heating to 350 °C in an inert atmosphere, for approximately 5 h. Next, access holes with a diameter of 40 µm were created through the PI layer with picosecond laser drilling. An Nd:YAG laser with a third harmonic generation module was used (355 nm, Duetto, Time-Bandwidth Products), with parameters set to 10 iterations at a repetition rate of 50 kHz, total average power of 20 mW, and scanning speed of 60 mm/s. The next phase involved copper sputtering and lithographic patterning. To improve adhesion, the PI surface was slightly roughened by performing reactive-ion etching (RIE) with a gas mixture of O_2 and CHF_3 for 1 min. The RIE step also assisted in the removal of any minimal redeposited, decomposed PI material from the pad surface, following via drilling. Then, a 25 nm layer of TiW and a 1 µm layer of Cu were sputtered. Electrical tracks were defined on this uniform Cu layer by photolithographic patterning of a positive-tone photoresist (AZ4562, MicroChemicals), followed by metal etching. The fully embedded sample is shown in Fig. 5.

2.2.3. Optical characterization of the integrated arrays

To accurately design the micro-optic elements, it is essential to characterize the emission properties of the individual lasers (emitters) within the integrated VCSEL arrays. Specifically, we require precise data on the wavelength, near-field beam profile, and polarization across various driving currents, as well as verification of stable intensity over time. First, the operation of the VCSEL was verified by measuring the optical output power (L) and voltage (V) along the full operational current extent (I). The power was captured by coupling into a 50 µm core-NA 0.2 multimode fiber connected to a power meter (Thorlabs, PM400). The L-V-I curves are shown in Fig. 6(a). The regime in which each VCSEL operates in single-mode was identified by analyzing the emission spectrum across a range of driving currents. Secondary modes were distinguished by the appearance of additional peaks in the spectrum as shown in Fig. 6(b). The measurements were conducted using an optical spectrum analyzer (Agilent 86142B). The single-mode operation current range was determined for each emitter, with peak emission wavelengths centered around 846 nm. The VCSEL beam was then captured at the near field using a beam profiler consisting of a 40 × NA 0.65 microscope objective, a prism-based variable optical attenuator, and a Charge-Coupled Device (CCD) camera (SP620U by Ophir-Spiricon). The near-field profiling revealed a beam diameter of approximately 2.8 µm. Additionally, by interposing a rotating polarizing filter, the linear polarization was found to be oriented along the long side of the array (X-polarization).

Additionally, the integration process may induce mechanical stress to VCSEL arrays. Stress-induced strain can affect VCSEL emission characteristics, particularly wavelength and polarization [47]. Therefore, comparing post-integration characterization results to a pre-integration reference is essential. Establishing a reliable pre-integration reference was not feasible, as direct electrical probing of the VCSEL pads prior to integration introduces mechanical stress to the chip, contrary to post-integration measurements via copper fanout probing. As an alternative, we compared the post-integration spectra, L-V-I characteristics, and polarization with the values provided by the manufacturer. The post-integration electro-optical characteristics matched the reference data closely, suggesting that the integration process does not significantly alter device performance. For completeness, it is important to emphasize

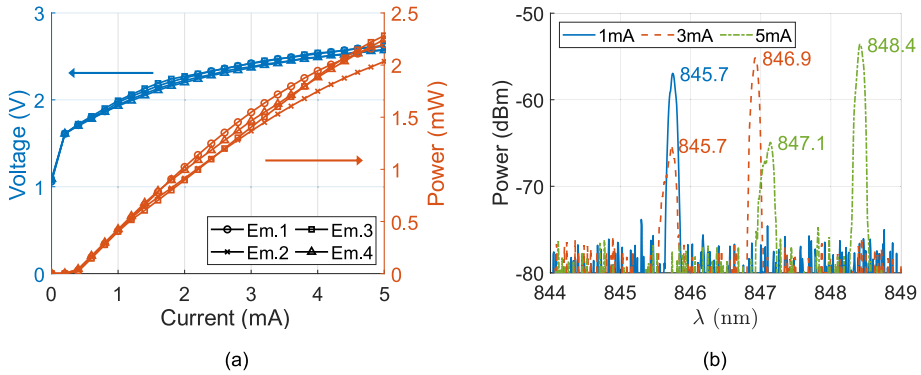

Fig. 6. Experimental emission characteristics of a fully embedded VCSEL array. (a) L-V-I curves for the four emitters within a single array (Em.1–Em.4, from left to right in the physical layout, as depicted in Fig. 5). (b) Emission spectra of a VCSEL at 1 mA, 3 mA, and 5 mA. The emergence of a secondary mode at higher currents is evident, as well as the known wavelength dependency on current intensity.

that this conclusion is based on L-V-I characteristics and spectra acquired under direct current operation, and the polarization of the primary mode—manifesting for low current values. Other VCSEL performance aspects relating to optical response under signal modulation, such as modulation bandwidth, were not assessed in this study. Finally, intensity stability over time was quantified with optical power measurements spanning a few minutes, for various driving currents within the previously identified single-mode regime. The coefficient of variation was systematically below 1 %, confirming stable emission over time.

3. Design of micro-optic focusing elements

We designed two types of focusing lenses—refractive and diffractive—to match the 5 μm mode field diameter (MFD) of an SMF at 850 nm (Thorlabs, 780HP). An ideal refractive interface is formed by a continuous surface, whereas a diffractive surface presents abrupt height discontinuities along the optical propagation direction. These two inherently different geometries were chosen to highlight the design versatility which 2PP-DLW offers as a fabrication technique. To evaluate the design performance, we used the modal overlap integral (OI)—calculated with the fundamental mode of an SMF—as the primary merit function. For the diffractive element—being inherently more susceptible to losses—we also monitored the conversion efficiency and the signal-to-noise ratio (SNR) to ensure sufficient light was directed to the region of interest. For the definitions and more details about the above-mentioned merit functions, see Appendix A.

3.1. Diffractive microlens

In order to achieve adequate phase modulation, it is necessary to increase the beam diameter before introducing it into the diffractive surface. To efficiently capture the impinging light, the diffractive surface should be sufficiently larger than the expanded beam. On the other hand, the lateral extent of the 2PP-printed micro-optics must be smaller than 125 μm, allowing fabrication on adjacent emitters situated at a pitch of 250 μm. These considerations led to the choice of an expanded beam diameter of 50 μm and a diffractive lens diameter of 100 μm, resulting in an analytically calculated loss of less than 0.04 % of the impinging light. The simplest way to achieve the intended beam expansion is to let the VCSEL beam expand in a uniform medium as dictated by the Gaussian beam propagation equation in free space (Eq. 1, [48]).

$$w(z) = w_0\left[1 + \left(\frac{\lambda z}{\pi w_0^2}\right)^2\right]^{1/2} \tag{1}$$

where $w(z)$ is the beam radius, w_0 is the beam waist radius, λ is the wavelength of the beam in the medium, and z is the distance from the beam waist plane. The refractive index of the medium (≈1.544 at 846 nm) is a

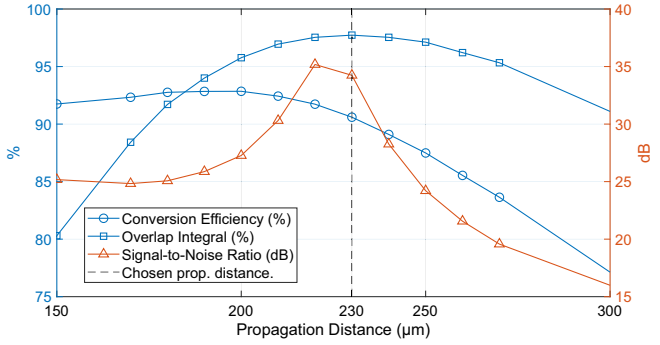

Fig. 7. Merit functions for different implementations of the IFTA at various propagation distances. The optimal OI of ≈97 % is achieved at a propagation distance of 230 μm, indicated by the dashed line. At this distance, the conversion efficiency remains above 90 %, and the SNR shows higher values in the same region, ensuring an adequate amount of light is directed into the area of interest.

first order interpolation based on data from Nanoscribe [49] and literature [50] for fully cured IP-Dip2, at 589 nm and 1550 nm, respectively. Based on (1), the required expansion region thickness is calculated to be 200 μm.

We designed the diffractive element using the Iterative Fourier Transform Algorithm (IFTA) [51] with VirtualLab Fusion (LightTrans). The IFTA iteratively applies Fourier and inverse Fourier transforms to determine the phase retardation profile required at a given input field to achieve a desired output field over a specified propagation distance. Then, the phase map is turned into a height profile based on the thin-element approximation, as shown in our previous work [52]. While not the simplest or fastest method for designing a diffractive focusing lens in the paraxial regime, the IFTA's flexibility and compatibility with beam splitting and complex beam shaping make it well-suited for our future work. The design of the focusing lens comprises eight discrete levels—as an optimal compromise between performance and fabrication time—and a lateral resolution of 200 nm. Evaluating the design algorithm across multiple propagation distances revealed an optimal distance of 230 μm, where the diffractive element focuses the expanded beam down to a 5.2 μm diameter spot. At this distance, the evaluation metrics conversion efficiency, SNR, and OI were 90.2 %, 34.1 dB, and 97 %, respectively, as shown in Fig. 7.

3.2. Refractive microlens

For the refractive microlens design we used the Physical Optics Propagation engine of Zemax OpticStudio. To match the diffractive counterpart, the lens' total height was set to 200 μm and the propagation distance (i.e. the distance from the lens vertex to the focal plane) was set

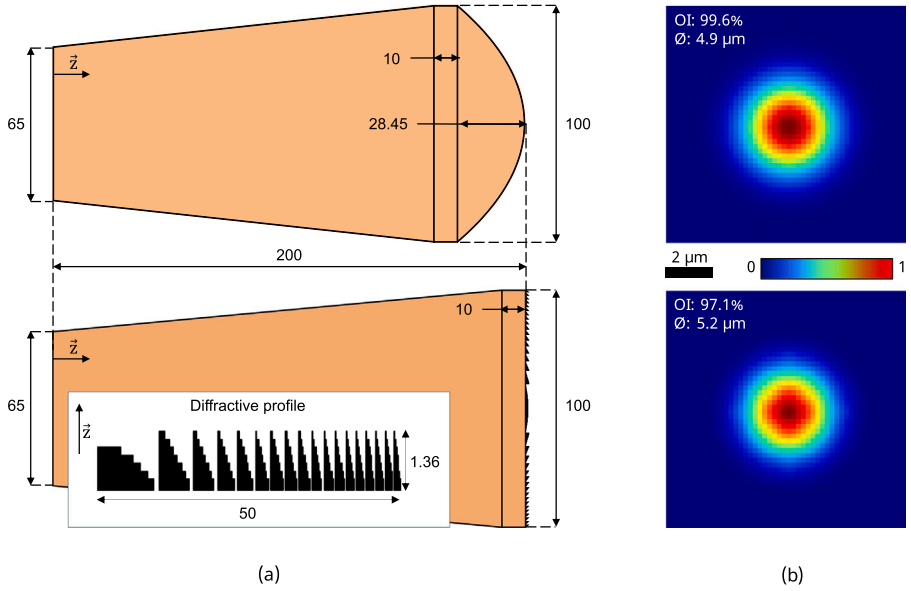

Fig. 8. (a) To-scale cross-section schematics of the refractive element (top) and the diffractive element (bottom). The inset illustrates the diffractive microlens profile (not to scale). The vector $\vec{z}$ indicates the beam propagation direction. All dimensions are in µm. (b) Corresponding normalized intensity of output beam profiles at their focal planes. The diameter symbol (⌀) denotes the $1/e^2$ normalized intensity diameter.

to 230 µm. Leveraging the design flexibility of 2PP-DLW we improved the microlens performance by changing the optical surface geometry from spherical to aspherical, as described by Eq. (2).

$$Z_{sag} = \frac{r^2/R_c}{1+\sqrt{1-(1+k)(r/R_c)^2}} \tag{2}$$

where Z_{sag} is the sagitta of the lens, R_c is the radius of curvature, r is the radial lens distance from its vertex, and k is the conic constant. Exploring the parameter space, we found an optimal combination to be $R_c = -45$ µm and $k = -0.925$, achieving a focal spot beam diameter of 4.9 µm and an overlap integral of 99.6 %. The optimized micro-optics are shown in Fig. 8.

4. Fabrication and characterization of focusing microlenses

4.1. Fabrication optimization on planar substrates

Before nanoprinting on the embedded chips, the 2PP parameters were optimized on silanized fused silica substrates. We made use of the Photonic Professional GT+ system, and the IP-Dip2 photoresist, from Nanoscribe [49]. The exposure dose (energy absorbed per unit volume) was varied by combining different scanning speeds (1 mm/s–40 mm/s) with varying laser power (10 %–70 %), the latter expressed as a fraction of the maximum average laser power the system can deliver (≈50 mW). We used the highest NA objective lens available (63×, NA 1.4) in the dip-in laser lithography (DiLL) configuration to achieve the finest feature definition, which is especially important for the height discontinuities of the diffractive structures. After printing, the microlens arrays were developed by immersion in propylene glycol methyl ether acetate (PGMEA) for 20 min and rinsed with isopropanol.

We measured the height profile with WLI and compared it with the designed geometry. We found that, generally, as the exposure dose increased, the fabricated geometry more closely matched the design. However, increasing the dose was limited by the emergence of micro-explosions and micro-bubble formation at elevated laser powers due to overexposure. Although the micro-bubbles do not necessarily affect the quality of the lens surface, they introduce beam distortions as the beam propagates through the improperly polymerized medium. Therefore, we chose the highest dose that systematically did not lead to overexposure. Under these conditions, the exposure of a refractive and a diffractive microlens was completed in 19 and 17 min, respectively. The topography characterization results are shown in Fig. 9.

4.2. On chip fabrication

With the optimal 2PP-DLW parameters determined, we proceeded with the fabrication of the micro-optics on the embedded chips, using DiLL. To ensure adhesion when printing on low refractive index substrates, it is a standard practice to initiate writing slightly within the substrate and gradually move the focal plane outward. However, this approach was unsuitable for VCSELs due to the reflective nature of the top distributed Bragg reflector, which caused beam reflection, self-interference, and thus regions of higher energy, leading to overexposure at otherwise optimal dose parameters. To address this, the first polymerized layer was very accurately placed within the thin PI layer above the emitter rather than directly onto it. Additionally, the laser power was reduced by ≈3 % for the first 5–10 µm at the base of our structures. The resulting structures are shown in Fig. 10.

The alignment of the fabricated microlenses relative to the underlying VCSELs was assessed using WLI measurements. The average angular misalignment—defined as the angle between the substrate normal and the microlens symmetry axis—was found to be 3.1 ± 0.7° (n = 10). Based on our simulations, this level of misalignment mainly results in a lateral shift of the focal spot on the focal plane by ≈12 µm, which would significantly impact SMF coupling efficiency. However, for our application—free-space coupling into an SMF—this issue can be easily mitigated by adjusting the position and orientation of the collecting SMF. As a reference, respective simulations at an angular misalignment of 3.5° showed that proper SMF repositioning can recover the coupling efficiency, reducing the loss to 2.2 % for the refractive microlens and 4.9 % for the diffractive microlens, relative to the perfectly aligned configuration.

4.3. Beam profiling and fiber coupling

To begin with, we utilized the beam profiling setup described in Section 2.2.3. The beam profile was captured at various distances by translating the beam profiler along the propagation direction (Z-axis).

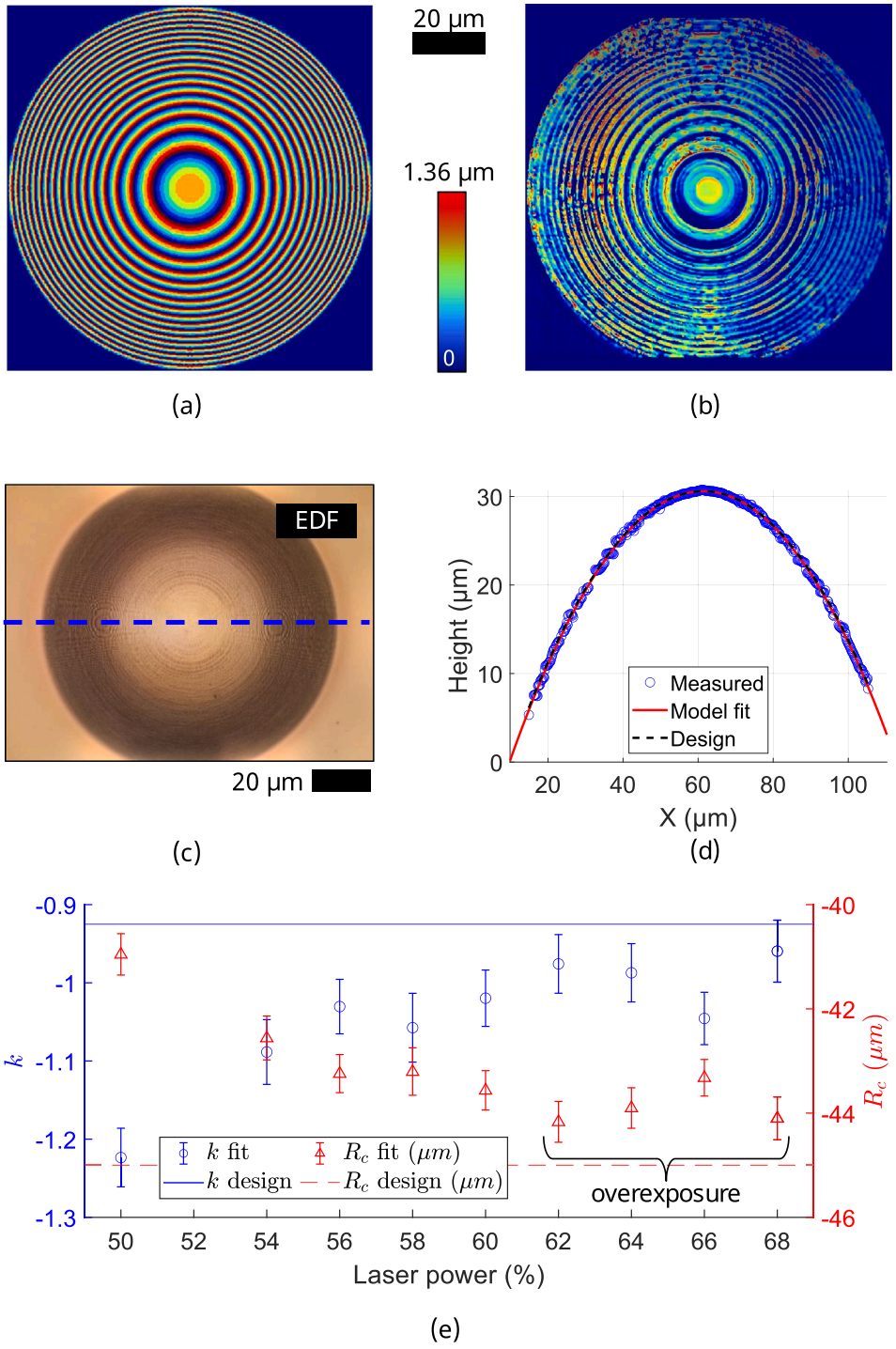

Fig. 9. Topography characterization with WLI for microlenses printed on glass substrates. The designed and processed measured height profile of the diffractive lens is shown in (a) and (b), respectively. More information about the processing of (b) can be found in the supplementary material (SM1). (c) An extended-depth-of-focus (EDF) microscope image of the refractive lens. A profile line is drawn through its vertex (dashed). In (d), the corresponding WLI profile line data is fitted with the aspheric model Eq. (2) to reveal the parameters R_c, k. Note that the fitted line and the design are indiscernible due to their excellent match. The fitted parameters—with the 95 % confidence intervals as error bars—are plotted against different laser powers (with laser scanning speed fixed at 40 mm/s). For doses corresponding to laser powers above or equal to 62 %, overexposure was observed during polymerization.

At each position, the beam profile was recorded, and the beam diameter was determined by fitting a circle to the $1/e^2$ normalized intensity points. The diffractive and refractive lenses produced focal spot diameters of 5.1 µm and 5.0 µm, respectively, with a corresponding OI of 98.5 % and 99.3 %. These results are summarized in Fig. 11.

For fiber coupling, we first used a multimode fiber (OM4 50/125 MM) connected to a photodiode (S120C) and a power meter (Thorlabs, PM400). The VCSELs were driven within their single-mode regime, with the multimode fiber positioned close to the lenses to maximize coupling efficiency. Each measurement lasted 2–5 minutes, establishing

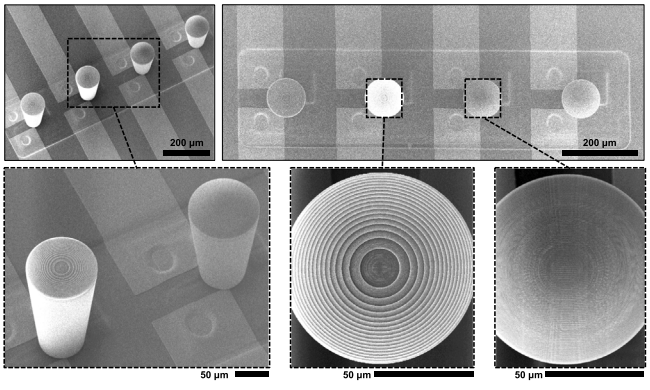

Fig. 10. Scanning electron microscope imaging of the refractive and diffractive microlenses fabricated using 2PP-DLW on a fully integrated functional VCSEL.

a reference for the coupled power (P_{REF}), which ranged from 150 to 400 µW at 0.6–1.0 mA. The coefficient of variation over time was less than 1 %, indicating stable power measurements after 2PP-printing of the micro-optics on top of the VCSELs.

Subsequently, a Thorlabs 780HP SMF was aligned with the microlenses, and the power was similarly measured (P_{SMF}). The SMF coupling efficiency η_c was calculated as $\eta_c = P_{SMF}/P_{REF}$. We achieved an optimal η_c of 0.83 ± 0.011 for the diffractive lens and 0.99 ± 0.007 for the aspheric lens. The uncertainty figures denote the propagated error over time. The superior performance of the refractive lens in terms of coupling efficiency can likely be attributed to its reduced susceptibility to scattering and far-field distortions, effects that are more prominent in diffractive elements. Specifically, light captured by the multimode fiber (NA 0.2) is not captured by the single-mode fiber (NA 0.13), which impacts the coupling efficiency to the latter.

5. Conclusion

We demonstrated the face-up integration of VCSEL arrays with 3D nanoprinted micro-optics, utilizing FLICE-fabricated fused silica microwells and two-photon polymerization-based direct laser written micro-optics. The high lasing accuracy combined with the superior KOH selectivity facilitated the precise definition of the housing microwells with an accuracy of 1 µm. This allowed for accurate chip insertion and bonding (maximum feature protrusion of ≈2.4 µm) and minimal chip tip/tilt (less than 0.4°). The arrays were covered and electrically interconnected with an ERDL, which was fabricated through a multi-step

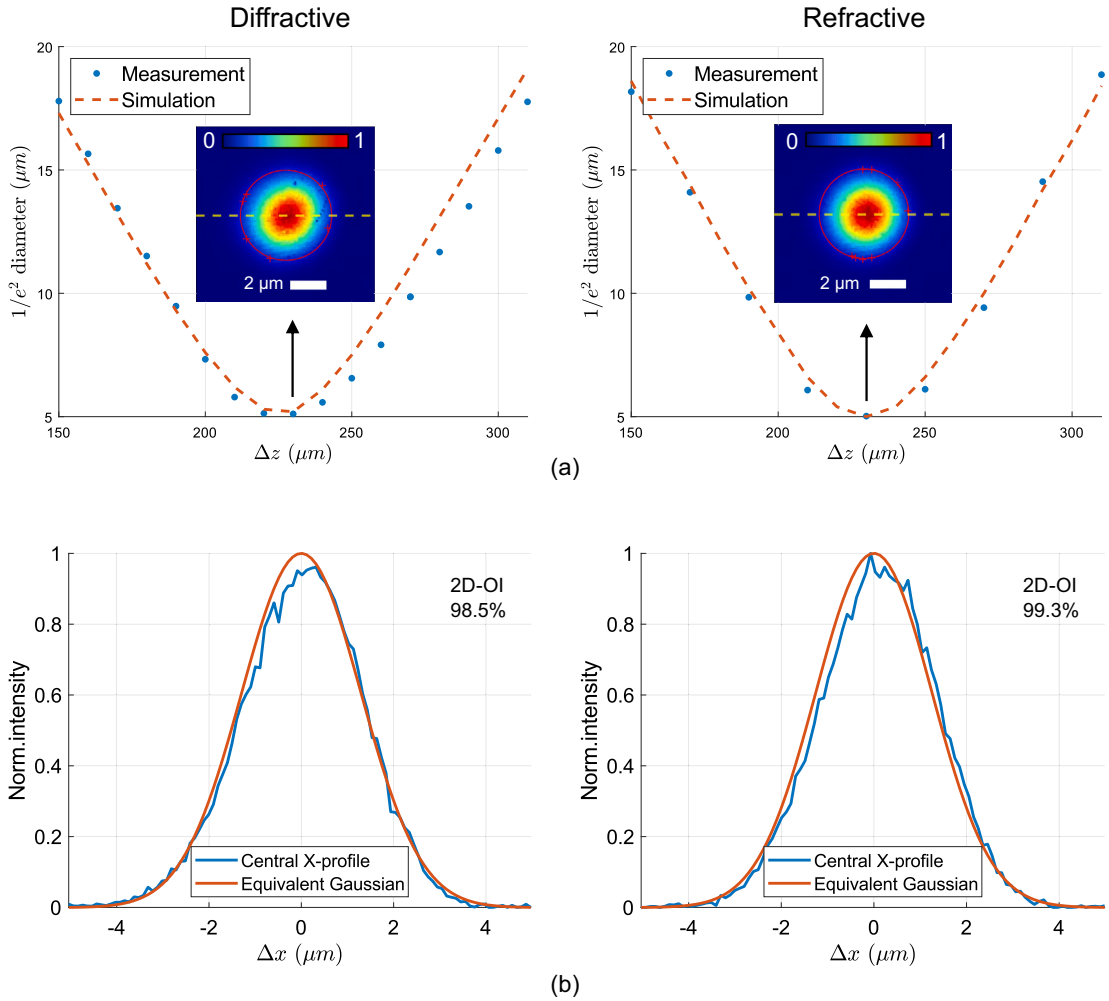

Fig. 11. Characterization of the VCSEL beams focused by diffractive and refractive microlenses. (a) The measured beam diameter is plotted along the propagation direction and compared with the simulations. The beam spot size reaches a minimum at the focal plane of the microlenses. The insets show the normalized intensity distribution at the focal plane, with a horizontal X-profile line drawn. (b) At the focal plane, the X-profile is compared with an equivalent Gaussian beam having the same full width at half maximum (FWHM). The 2D modal overlap integral between the measured beam intensity profile and a 2D Gaussian beam with an MFD of 5 µm is also calculated, yielding overlap values of 98.5 % (diffractive) and 99.3 % (refractive), demonstrating good Gaussian-like beam quality.

process comprising substrate silanization, spin-coating and curing of a ≈5.5 μm thick PI layer, picosecond laser microvia drilling, RIE, TiW/Cu sputtering, and photolithography. Optical characterization of the VCSEL emission confirmed stable power over time (relative standard deviation <1 %), and identified key beam attributes: 2.8 μm waist diameter, X-polarization, and single-mode operation for driving current intensities of 0.6–1.0 mA, at a wavelength of 846 nm. Additionally, comparison with manufacturer-supplied values indicates a strong match between pre- and post-integration characteristics, suggesting that the integration process does not introduce significant strain on the embedded devices.

Subsequently, diffractive and refractive microlenses were designed to efficiently focus the integrated VCSEL beams for SMF coupling. Both elements have a total height of 200 μm, a diameter of 100 μm and focus the beam to a 5 μm diameter spot over a propagation distance of 230 μm. After optimizing the nanoprinting parameters on planar glass substrates, the microlenses were fabricated directly on top of the embedded arrays using 2PP-DLW. Using WLI, a misalignment of about 3° was measured between the microlenses and the substrate normal, indicating that proper SMF repositioning would be necessary for efficient coupling—at a cost of roughly 2 %–5 % relative to the ideally aligned case. The consistent misalignment direction, both within individual substrates and across different substrates, suggests a systematic source related to the printing setup. However, since substrate tilt correction is a standard feature in state-of-the-art equipment, we did not explore the alignment improvement further.

Subsequently, the focused beams were characterized using a CCD-based beam profiler, confirming efficient focusing. Specifically, at the focal plane, the refractive and diffractive elements achieved spot diameters of 5.1 μm and 5.0 μm, respectively. The overlap integral with the mode field of a single-mode fiber (5 μm MFD Gaussian) was calculated, yielding values of 98.5 % for the refractive element and 99.3 % for the diffractive element. Finally, the SMF coupling efficiency was evaluated, achieving optimal values of 0.83 ± 0.011 and 0.99 ± 0.007 for the diffractive and refractive microlenses, respectively. It is worth noting that although both microlenses achieve the desired 5 μm diameter spot at the designed focal distance, the diffractive one exhibits inferior SMF coupling performance. This is attributed to increased scattering, suggesting that the refractive counterpart would be more suitable for applications where optical losses mitigation is critical.

To conclude, by combining the flexibility of 2PP-DLW with the advantages of face-up assembly on a glass interposer, this approach presents a possible solution for compact, high-density photonic systems. Future work could explore more complex micro-optic designs for simultaneous coupling of multiple emitters into in-plane waveguides or photonic integrated circuits – with the use of photonic wire-bonds, for instance. An additional natural direction would be extending the presented methodology to larger VCSEL arrays. The simultaneous operation of multiple devices could challenge the thermal management capabilities of the glass interposer and should be preceded by a thorough assessment of heat dissipation and long-term reliability. Furthermore, future work may extend the investigation beyond direct-current operation and assess the high-speed performance characteristics of the integrated VCSELs to evaluate their suitability for data communication applications, compared to unpackaged ones. Finally, further integration of VCSEL drivers and signal modulation capabilities could expand its application scope in VCSEL-based co-packaged optics solutions.

CRediT authorship contribution statement

Athanasios Kyriazis: Writing – review & editing, Writing – original draft, Visualization, Validation, Software, Methodology, Investigation, Formal analysis, Data curation. **Salah Guessoum:** Validation, Methodology, Investigation, Formal analysis. **Jeroen Missinne:** Writing – review & editing, Software, Resources, Methodology, Formal analysis. **Martin Virte:** Writing – review & editing, Supervision, Resources, Project administration, Methodology, Funding acquisition, Conceptualization. **Jürgen Van Erps:** Writing – review & editing, Supervision, Resources, Project administration, Methodology, Funding acquisition, Conceptualization. **Geert Van Steenberge:** Writing – review & editing, Supervision, Resources, Project administration, Methodology, Funding acquisition, Conceptualization.

Declaration of competing interest

The authors declare that they have no known competing financial interests or personal relationships that could have appeared to influence the work reported in this paper.

Acknowledgments

This work was financially supported by Fonds Wetenschappelijk Onderzoek (G020621N), Interreg (NWE758 “OIP4NWE”, “Fotonica Pilootlijnen”), Methusalem Foundation, IOF and OZR of Vrije Universiteit Brussel.

We would like to acknowledge the assistance of the CMST support team, and especially thank Viktor Geudens, Steven Van Put, Rik Verplancke, and Koen Vanmol on the B-PHOT side.

Appendix A. Merit functions

When comparing the output field to the desired one, we make use of merit functions, to assess the optical system by expressing its performance as a single number. We succinctly present the merit functions that are used in our work. Since the definitions slightly vary in literature, we will follow the way merit functions are calculated in the software mostly used for the diffractive design (VirtualLab, LightTrans) [53].

In the definitions below, we assume a desired output field (U_D) and an input field (U_{in}); U is used to denote power. The diffracted output field (U_{out}) is projected in the window that contains the evaluation/signal/desired region (D). This is typically the optimization region, slightly larger than the desired focal spot. The complex optimal scale factor is a type of average value and is calculated as:

$$a = \frac{I_{out\cdot D}}{I_D} \tag{A.1}$$

where $I_{out\cdot D} = \int_D |U_{out}||U_D|$ and $I_D = \int_D |U_D|^2$. $\int_D$ denotes integration over the signal region, whereas $\int$ will indicate integration over the whole field plane.

Conversion efficiency (CE). Measures the portion of the incident field's power (U_{in}) that flows into the signal area (D):

$$CE = |a|^2 \frac{I_D}{I_{in}} \tag{A.2}$$

where $I_D = \int_D |U_D|^2$ and $I_{in} = \int |U_{in}|^2$.

Signal to noise ratio (SNR). Shows the correspondence between the desired output field (U_D) and another, noise-affected field (U_{out}):

$$\mathrm{SNR} = \frac{I_{out}}{I_{noise}} \tag{A.3}$$

where $I_{out} = \int_D |U_{out}|^2$ and $I_{noise} = \int_D \left(|U_{out}| - a|U_D|\right)^2$. It is usually expressed in dB as $10 \cdot \log_{10}(\mathrm{SNR})$.

Overlap integral (OI). It is not one of the merit functions usually used in the general design and optimization of diffractive structures, but it provides a useful comparison between two light distributions (such as the matching of optical modes) and is used in this work. Let $E_D(x, y)$, $E_{out}(x, y)$ be the desired and output field, the overlap integral is given by:

$$\eta = \mathrm{OI} = \frac{|\iint E_D^* \cdot E_{out}\ \mathrm{dxdy}|^2}{\iint |E_D|^2\ \mathrm{dxdy} \iint |E_{out}|^2\ \mathrm{dxdy}} \tag{A.4}$$

where $*$ denotes the complex conjugate.

Appendix B. Supplementary data

Supplementary data to this article can be found online at doi:10.1016/j.optlastec.2025.113415.

Data availability

Data will be made available on request.

References

[1] C. Minkenberg, R. Krishnaswamy, A. Zilkie, D. Nelson, Co-packaged datacenter optics: opportunities and challenges, IET Opto. Electron. 15 (2) (2021) 77–91.

[2] X. Shen, B. Chen, Y. Zhu, W. Shi, Silicon photonic integrated circuits and its application in data center, in: Seventh Symposium on Novel Photoelectronic Detection Technology and Applications, vol. 11763, SPIE, 2021, pp. 2110–2123.

[3] A. Boletti, P. Boffi, P. Martelli, M. Ferrario, M. Martinelli, Performance analysis of communication links based on VCSEL and silicon photonics technology for high-capacity data-intensive scenario, Opt. Express 23 (2) (2015) 1806–1815.

[4] F. Koyama, High-speed VCSEL photonics for datacenter networks, in: Semiconductor Lasers and Laser Dynamics X, vol. PC12141, International Society for Optics and Photonics, SPIE, 2022, https://doi.org/10.1117/12.2627093, p. PC1214104. https://doi.org/10.1117/12.2627093.

[5] G. Kanakis, N. Iliadis, W. Soenen, B. Moeneclaey, N. Argyris, D. Kalavrouziotis, S. Spiga, P. Bakopoulos, H. Avramopoulos, High-speed VCSEL-based transceiver for 200 GBE short-reach intra-datacenter optical interconnects, Appl. Sci. 9 (12) (2019) 2488.

[6] B. Wang, W.V. Sorin, P. Rosenberg, L. Kiyama, S. Mathai, M.R. Tan, 4 × Gbps/fiber CWDM VCSEL arrays for co-packaged interconnects, J. Lightwave Technol. 38 (13) (2020) 3439–3444.

[7] H. Chen, C. Li, N.K. Fontaine, B. Farah, C. Bolle, R. Ryf, M. Mazur, L. Dallachiesa, D.T. Neilson, O. Raz, et al., 10-mode-multiplexed transmitter employing 2-D VCSEL matrix, in: 2021 European Conference on Optical Communication (ECOC), IEEE, 2021, pp. 1–4.

[8] C. Li, H. Chen, N.K. Fontaine, B. Farah, C. Bolle, R. Ryf, M. Mazur, O. Raz, C. Neumeyr, J.C. Alvarado, et al., Co-packaged optics with multimode fiber interface employing 2-D VCSEL matrix, J. Lightwave Technol. 40 (10) (2022) 3325–3330.

[9] L. Dong, X. Gu, S. Hu, F. Koyama, Densely packed 1.1 μm band vertical cavity surface emitting laser array for co-packaged optics, Jpn J. Appl. Phys. 61 (SK) (2022) SK1011, https://doi.org/10.35848/1347-4065/ac64e3.

[10] T. Yagisawa, M. Miyoshi, J. Miike, T. Azuma, Y. Harada, S. Ide, K. Morito, Novel packaging structure using VCSEL array and multi-core fiber for co-packaged optics, in: 2022 IEEE CPMT Symposium Japan (ICSJ), IEEE, 2022, pp. 9–12.

[11] W. Yoshida, Y. Ishige, K. Nagashima, H. Nasu, 56-gb/s pam4 × 8-channel VCSEL-based optical transceiver for co-packaged optics, in: 2022 IEEE CPMT Symposium Japan (ICSJ), IEEE, 2022, pp. 1–4.

[12] D.M. Kuchta, Developments of VCSEL-based transceivers for co-packaging, in: Optical Fiber Communication Conference (OFC) 2023, Optica Publishing Group, 2023, https://doi.org/10.1364/OFC.2023.M4E.6, https://opg.optica.org/abstract.cfm?URI=OFC-2023-M4E.6.

[13] W. Tian, H. Hou, H. Dang, X. Cao, D. Li, S. Chen, B. Ma, Progress in research on co-packaged optics, Micromachines 15 (10) (2024) 1211, https://doi.org/10.3390/mi15101211, https://www.mdpi.com/2072-666X/15/10/1211.

[14] H. Schröder, J. Schwietering, G. Böttger, V. Zamora, Hybrid photonic system integration using thin glass platform technology, J. Opt. Microsyst. 1 (3) (2021) 033501, https://doi.org/10.1117/1.JOM.1.3.033501.

[15] K. Burt, J. Ahadian, C. Bohn, J. Coronati, M. Epitaux, A. Owens, N. Robertson, S. Skendzic, High density optical transceiver packaging using glass substrates and through glass vias, in: 2023 IEEE CPMT Symposium Japan (ICSJ), 2023, pp. 37–40, https://doi.org/10.1109/ICSJ59341.2023.10339635.

[16] P. Gupta, A. Tanwar, X. He, K. Gradkowski, K.M. Razeeb, P.E. Morrissey, P. O'Brien, Substrate integrated micro-thermoelectric coolers in glass substrate for next-generation photonic packages, J. Opt. Microsyst. 4 (1) (2024) 011006, https://doi.org/10.1117/1.JOM.4.1.011006.

[17] K. Nieweglowski, T. Tiedje, D. Schöniger, R. Henker, F. Ellinger, K. Bock, Electro-optical integration for VCSEL-based board-level optical chip-to-chip communication, in: Other Conferences, 2017, https://api.semanticscholar.org/CorpusID:114107027.

[18] H. Schröder, O. Kirsch, D. Weber, H. Thiem, Photonic system integration by applying microelectronic packaging approaches using glass substrates, in: 2023 IEEE 73rd Electronic Components and Technology Conference (ECTC), 2023, pp. 216–223, https://doi.org/10.1109/ECTC51909.2023.00045.

[19] L. Brusberg, J.R. Grenier, A.R. Zakharian, L.W. Yeary, S.-H. Seok, J.-H. Noh, Y.-G. Kim, J. Matthies, C.C. Terwilliger, B.J. Paddock, et al., Glass platform for co-packaged optics, IEEE J. Sel. Top. Quantum Electron. 29 (2023) 1–10.

[20] K. Kaur, Flip-chip bonding of vertical-cavity surface-emitting lasers using laser-induced forward transfer, Appl. Phys. Lett. 104 (6) (2014).

[21] Q. Li, V. Raimbault, P.-F. Calmon, B. Reig, P. Debernardi, H. Ottevaere, J.-B. Doucet, J. Roul, V. Bardinal, Direct 3D-printing of microlens on single mode polarization-stable VCSEL chip for miniaturized optical spectroscopy, J. Opt. Microsyst. 3 (3) (2023) 033501, https://doi.org/10.1117/1.JOM.3.3.033501.

[22] M.-J. Lu, S.-Y. Mu, C.-S. Cheng, J. Chen, Advanced packaging technologies for copackaged optics, in: 2022 IEEE 72nd Electronic Components and Technology Conference (ECTC), IEEE, 2022, pp. 38–42.

[23] E. Bosman, G. Van Steenberge, B. Van Hoe, J. Missinne, J. Vanfleteren, P. Van Daele, Highly reliable flexible active optical links, IEEE Photonics Technol. Lett. 22 (5) (2010) 287–289, https://doi.org/10.1109/LPT.2009.2038797.

[24] E. Bosman, J. Missinne, B.V. Hoe, G.V. Steenberge, S. Kalathimekkad, J.V. Erps, I. Milenkov, K. Panajotov, T.V. Gijseghem, P. Dubruel, H. Thienpont, P.V. Daele, Ultrathin optoelectronic device packaging in flexible carriers, IEEE J. Sel. Top. Quantum Electron. 17 (3) (2011) 617–628, https://doi.org/10.1109/JSTQE.2010.2096407.

[25] P. Maier, Y. Xu, M. Trappen, M. Lauermann, A. Henniger-Ludwig, H. Kapim, T. Kind, P.-I. Dietrich, A. Weber, M. Blaicher, C. Wurster, S. Randel, W. Freude, C. Koos, 3d-printed facet-attached optical elements for connecting VCSEL and photodiodes to fiber arrays and multi-core fibers, Opt. Express 30 (26) (2022) 46602–46625, https://doi.org/10.1364/OE.470676, https://opg.optica.org/oe/abstract.cfm?URI=oe-30-26-46602.

[26] J.H. Brannon, J.R. Lankard, A.I. Baise, F. Burns, J. Kaufman, Excimer laser etching of polyimide, J. Appl. Phys. 58 (5) (1985) 2036–2043, https://doi.org/10.1063/1.336012, https://pubs.aip.org/aip/jap/article-pdf/58/5/2036/18412743/2036_1_online.pdf.

[27] R.M. Carter, J. Chen, J.D. Shephard, R.R. Thomson, D.P. Hand, Picosecond laser welding of similar and dissimilar materials, Appl. Opt. 53 (19) (2014) 4233–4238, https://doi.org/10.1364/AO.53.004233, https://opg.optica.org/ao/abstract.cfm?URI=ao-53-19-4233.

[28] B.N. Chichkov, C. Momma, S. Nolte, F.V. Alvensleben, A. Tünnermann, Femtosecond, picosecond and nanosecond laser ablation of solids, Appl. Phys. A 63 (2) (1996) 109–115.

[29] K.M. Davis, K. Miura, N. Sugimoto, K. Hirao, Writing waveguides in glass with a femtosecond laser, Opt. Lett. 21 (21) (1996) 1729–1731, https://doi.org/10.1364/OL.21.001729, https://opg.optica.org/ol/abstract.cfm?URI=ol-21-21-1729.

[30] A. Marcinkevičius, S. Juodkazis, M. Watanabe, M. Miwa, S. Matsuo, H. Misawa, J. Nishii, Femtosecond laser-assisted three-dimensional microfabrication in silica, Opt. Lett. 26 (5) (2001) 277–279, https://doi.org/10.1364/OL.26.000277, https://opg.optica.org/ol/abstract.cfm?URI=ol-26-5-277.

[31] Y. Shimotsuma, P.G. Kazansky, J. Qiu, K. Hirao, Self-organized nanogratings in glass irradiated by ultrashort light pulses, Phys. Rev. Lett. 91 (24) (2003) 247405, https://doi.org/10.1103/PhysRevLett.91.247405, https://link.aps.org/doi/10.1103/PhysRevLett.91.247405.

[32] C.A. Ross, D.G. MacLachlan, D. Choudhury, R.R. Thomson, Optimisation of ultrafast laser assisted etching in fused silica, Opt. Express 26 (19) (2018) 24343–24356, https://doi.org/10.1364/OE.26.024343, https://opg.optica.org/oe/abstract.cfm?URI=oe-26-19-24343.

[33] A. Butkutė, T. Baravykas, J. Stančikas, T. Tičkūnas, R. Vargalis, D. Paipulas, V. Sirutkaitis, L. Jonušauskas, Optimization of selective laser etching (SLE) for glass micromechanical structure fabrication, Opt. Express 29 (15) (2021) 23487–23499, https://doi.org/10.1364/OE.430623, https://opg.optica.org/oe/abstract.cfm?URI=oe-29-15-23487.

[34] M.L. Choobbari, M. Vandermotten, T. Chalyan, I. Bihi, P. Gelin, W. De Malsche, W. Meulebroeck, L.A. van Grunsven, H. Thienpont, H. Ottevaere, An opto-acousto-fluidic microchip for efficient raman spectroscopy of microparticles in aqueous environment, Sens. Actuators B Chem. 418 (2024) 136300, https://doi.org/10.1016/j.snb.2024.136300, https://www.sciencedirect.com/science/article/pii/S092540052401030X.

[35] V. Geudens, S. Nategh, G. Van Steenberge, J. Belis, J. Missinne, Laser micromachined 3d glass photonics platform demonstrated by temperature compensated strain sensor, Opt. Laser. Technol. 169 (2024) 109970, https://doi.org/10.1016/j.optlastec.2023.109970, https://www.sciencedirect.com/science/article/pii/S0030399223008630.

[36] S. Maruo, O. Nakamura, S. Kawata, Three-dimensional microfabrication with two-photon-absorbed photopolymerization, Opt. Lett. 22 (2) (1997) 132–134, https://doi.org/10.1364/OL.22.000132, https://opg.optica.org/ol/abstract.cfm?URI=ol-22-2-132.

[37] H.-B. Sun, T. Kawakami, Y. Xu, J.-Y. Ye, S. Matuso, H. Misawa, M. Miwa, R. Kaneko, Real three-dimensional microstructures fabricated by photopolymerization of resins through two-photon absorption, Opt. Lett. 25 (15) (2000) 1110–1112, https://doi.org/10.1364/OL.25.001110, https://opg.optica.org/ol/abstract.cfm?URI=ol-25-15-1110.

[38] N. Lindenmann, G. Balthasar, D. Hillerkuss, R. Schmogrow, M. Jordan, J. Leuthold, W. Freude, C. Koos, Photonic wire bonding: a novel concept for chip-scale interconnects, Opt. Express 20 (16) (2012) 17667–17677, https://doi.org/10.1364/OE.20.017667, https://opg.optica.org/oe/abstract.cfm?URI=oe-20-16-17667.

[39] S. Schmidt, S. Thiele, A. Toulouse, C. Bösel, T. Tiess, A. Herkommer, H. Gross, H. Giessen, Tailored micro-optical freeform holograms for integrated complex beam shaping, Optica 7 (10) (2020) 1279–1286, https://doi.org/10.1364/OPTICA.395177, https://opg.optica.org/optica/abstract.cfm?URI=optica-7-10-1279.

[40] T. Baghdasaryan, K. Vanmol, H. Thienpont, F. Berghmans, T. Geernaert, J. Van Erps, Design and two-photon direct laser writing of low-loss waveguides, tapers and s-bends, J. Phys. Photonics 3 (4) (2021) 045001.

[41] T. Gissibl, S. Thiele, A. Herkommer, H. Giessen, Two-photon direct laser writing of ultracompact multi-lens objectives, Nat. Photonics 10 (8) (2016) 554–560.

[42] K. Vanmol, A.A.A. Nazar, H. Thienpont, F. Ferranti, J.V. Erps, Fabrication of multilevel metalenses using multiphoton lithography: from design to evaluation, Opt. Express 32 (6) (2024) 10190–10203, https://doi.org/10.1364/OE.514237, https://opg.optica.org/oe/abstract.cfm?URI=oe-32-6-10190.

[43] M. Kratz, M. Kniffler, C.L. Häfner, Influence of flexible multibeam intensity distributions on selective laser-induced etching process regimes, Opt. Express 32 (21) (2024) 36453–36468, https://doi.org/10.1364/OE.532425, https://opg.optica.org/oe/abstract.cfm?URI=oe-32-21-36453.

[44] Y. Bellouard, A. Champion, B. McMillen, S. Mukherjee, R.R. Thomson, C. Pépin, P. Gillet, Y. Cheng, Stress-state manipulation in fused silica via femtosecond laser irradiation, Optica 3 (12) (2016) 1285–1293, https://doi.org/10.1364/OPTICA.3.001285, https://opg.optica.org/optica/abstract.cfm?URI=optica-3-12-1285.

[45] C. Vanhaverbeke, R. Verplancke, J. De Smet, D. Cuypers, H. De Smet, Microfabrication of a spherically curved liquid crystal display enabling the integration in a smart contact lens, Displays 49 (2017) 16–25, https://doi.org/10.1016/j.displa.2017.05.005, https://www.sciencedirect.com/science/article/pii/S0141938217300069.

[46] R. Verplancke, M. Cauwe, D. Schaubroeck, D. Cuypers, B. Vandecasteele, L. Mader, C. Vanhaverbeke, M. Ballini, J. O'Callaghan, E. Goikoetxea, et al., Development of an active high-density transverse intrafascicular micro-electrode probe, J. Micromech. Microeng. 30 (1) (2019) 015010.

[47] S. Guessoum, A. Kyriazis, T. Malica, J. Van Erps, G. Van Steenberge, M. Virte, Wavelength tuning of VCSELsl via controlled strain, Optics Lett. 49 (15) (2024) 4477–4480.

[48] H. Kogelnik, T. Li, Laser beams and resonators, Appl, Opt. 5 (10) (1966) 1550–1567, https://doi.org/10.1364/AO.5.001550, https://opg.optica.org/ao/abstract.cfm?URI=ao-5-10-1550.

[49] Nanoscribe, Products, https://www.nanoscribe.com/en/products/, Accessed 2024.

[50] M. Schmid, D. Ludescher, H. Giessen, Optical properties of photoresists for femtosecond 3D printing: refractive index, extinction, luminescence-dose dependence, aging, heat treatment and comparison between 1-photon and 2-photon exposure, Opt. Mater. Express 9 (12) (2019) 4564–4577, https://doi.org/10.1364/OME.9.004564, https://opg.optica.org/ome/abstract.cfm?URI=ome-9-12-4564.

[51] R.W. Gerchber, W.O. Saxton, A practical algorithm for the determination of phase from image and diffraction plane pictures, OPTIK 35 (2) (1972) 237–246.

[52] A. Kyriazis, K. Vanmol, G.Y. Belay, H. Thienpont, J.V. Erps, Design, laser direct writing prototyping, and characterization of fan-out diffractive optical elements for optical interconnect applications, In A.M. Herkommer; G. von Freymann, M. Flury, (Eds.), 3D Printed Optics and Additive Photonic Manufacturing III, vol. 12135, International Society for Optics and Photonics, SPIE, 2022, https://doi.org/10.1117/12.2620785, p. 1213505.

[53] LightTrans, VirtualLab User's Manual (online), https://www.lighttrans.com/products-services/learning/users-manual.html (Accessed November 2024).